# In-Plane Hydrogen Bonds and Out-of-Plane Dipolar Interactions in Self-Assembled Melem Networks

Aldo Ugolotti, Valeria Lanzilotto,* Cesare Grazioli, Luca Schio, Jorge Manuel Zamalloa-Serrano, Matus Stredansky, Teng Zhang, Monica de Simone, Lorenzo Ferraro, Luca Floreano, Marcello Coreno, Carla Puglia, and Cristiana Di Valentin*

ABSTRACT: Melem (2,6,10-triamino-s-heptazine) is the building block of melon, a carbon nitride (CN) polymer that is proven to produce H_2 from water under visible illumination. With the aim of bringing additional insight into the electronic structure of CN materials, we performed a spectroscopic characterization of gas-phase melem and of a melem-based self-assembled 2D H-bonded layer on Au(111) by means of ultraviolet and X-ray photoemission spectroscopy (UPS, XPS) and near-edge X-ray absorption fine structure (NEXAFS) spectroscopy. In parallel, we performed density functional theory (DFT) simulations of the same systems to unravel the molecular charge density redistribution caused by the in-plane H-bonds. Comparing the experimental results with the spectroscopic DFT simulations, we can correlate the induced charge accumulation on the N_{amino} atoms to the red-shift of the corresponding N 1s binding energy (BE) and of the N_{amino} 1s → LUMO+n transitions. Moreover, when introducing a supporting Au(111) surface in the computational simulations, we observe a molecule−substrate interaction that almost exclusively involves the out-of-plane molecular orbitals, leaving those engaged in the in-plane H-bonded network rather unperturbed.
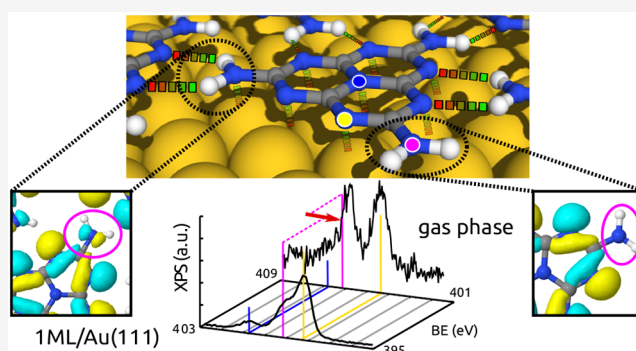
INTRODUCTION

Since the pioneering work of Wang et al.,[1] carbon nitride (CN) materials have been holding the stage among the plethora of organic polymers suitable for H_2 generation by photocatalytic water-splitting.[2−4] A prototype of CN materials is the Liebig's melon,[1,5] which derives from the linear polymerization of the melem molecule (2,6,10-triamino-s-heptazine). Along the polymer chain, secondary amino groups (−NH−) alternate with the s-heptazine cores, while one primary amino group (−NH_2) is preserved on each unit. Usually, melon is easily synthesized through the pyrolytic condensation of CNH precursors (e.g., cyanamide, dicyanamide, melamine, urea, thiourea) yielding amorphous or semicrystalline materials. Under peculiar synthesis conditions, melon can crystallize in graphitic-like structures, where the two-dimensional (2D) domains are stabilized by interchain H-bonding (NH⋯N) and interlayer $\pi−\pi$ interactions. A continuous 2D heptazine network exclusively based on covalent −NH− bridges (polyheptazine imide or PHI) has also been observed,[6] while isolation of the fully condensed polymer (only based on NC_3 connections) has not yet unambiguously been proven.

Notwithstanding the massive interest drawn by melon and related CN materials as polymeric photocatalysts for H_2 production, a clear understanding of the water-splitting mechanism is still missing nowadays.[7] In the two most discussed schemes, the CN acts either as (i) a classical semiconducting electrode photocatalyst for direct water-splitting[7,8] or as (ii) the photosensitizer in a chromophore−water adduct for a homolytic water-splitting through a proton-coupled electron transfer (PCET) reaction.[9,10] In the first case, the impinging light creates excitons that must then dissociate into free holes and electrons in order to trigger the surface reduction of protons and the surface oxidation of water, respectively. In the second case, a water molecule that is H-bonded to a photoexcited CN monomer decomposes into an OH radical through a PCET reaction; a second photon is then required to promote the release of the H atom transferred to the CN heterocycle. This latter model does not require the separation and the migration of free charges in the material, therefore it should promote a faster and a more efficient water-splitting mechanism. In the case of melem-based CN, there are

nominally four N-functionalities: pyridinic (N=C), primary (−NH$_2$), secondary (−NH−), and tertiary amino (NC$_3$) groups; however, their availability for the interaction with H$_2$O molecules depends on the specific structure of the polymer sample. For example, in Liebig's melon several amino groups (both −NH$_2$ and −NH−) are retained compared with the fully polymerized case; however, they are already interlocked with pyridinic N atoms through hydrogen bonds.

Several studies[9−12] proved that the optoelectronic properties of CN materials, such as the highly localized nature of the photoinduced excitons, are more related to those of their constituent monomers rather than to those of traditional semiconductors. This result would support a PCET-like mechanism, for which the pyridinic N atoms are expected to be the most favorable active sites due to their high availability in terms of stoichiometric ratio and good proton acceptor properties. Conversely, Lotsch and co-workers focus their attention on the role played by polymerization defects, such as terminal (−NH$_2$, −NH−) or other substitutional groups[13−15] as potential active sites.

In front of this puzzled scenario, it is paramount to achieve a detailed electronic characterization of CN-materials, considering the presence of both amino functionalities and hydrogen bonds. In this study we decided to simplify the system under investigation, given the difficulty of controlling the growth of a well-defined CN material, by considering a model H-bonded network, based on the self-assembling of gas phase CN-precursor molecules, whose deposition on a metal surface is more controllable.

In this context, some of us recently demonstrated the capability of core-level spectroscopies, such as X-ray photoemission (XPS) and near edge X-ray absorption fine structure spectroscopy (NEXAFS or XANES), to finely assess the electronic properties of the melamine molecule (the building block of another CN family, i.e. polytriazine-imide) in different conditions: (i) in the gas phase, as noninteracting molecule, (ii) condensed in H-bonded networks on Au(111),[16] and (iii) supported on Cu(111) while interacting with water.[17] Similarly, some of us theoretically investigated the properties of H-bonded and Cu-decorated melem-based polymers by simulating core-level spectra (XPS, NEXAFS), and infrared (IR) absorption spectra and their excitonic structure.[12,18,19]

In this work, we extend our methodology to the melem precursor by considering the molecules in the gas phase and after deposition/self-assembly on the Au(111) surface.[20−22] Our study is based on the comparison between experimental ultraviolet photoemission spectroscopy (UPS), XPS, and NEXAFS measurements and numerical simulations using density functional theory (DFT) methods. We analyze the intermolecular H-bond fingerprints in the core-level spectra by inspection of the charge redistributions occurring within the outer molecular orbitals, which are those more affected by the H-bonds formation. Moreover, by modeling unsupported and supported H-bonded melem 2D networks, we also clarify how the organo-catalyst electronic structure may be influenced by the coupling with an inorganic support.

■ METHODS

Experimental Methods. Most of the experiments were performed at the Elettra Synchrotron facility located in Trieste, Italy. Specifically, gas phase measurements were carried out at the GasPhase beamline. Melem was purchased from SynthonLab (purity 90%) and sublimed from a stainless steel crucible kept at 553 K. Before gas phase measurements, preliminary experiments for improving the powders purity were performed at the Surface Physics Laboratory at Uppsala University, Sweden. Purification required long-lasting degassing times, in ultrahigh-vacuum, by heating the powders at the molecule sublimation temperature. The effectiveness of the cleaning procedure was checked by measuring ultraviolet photoemission spectra of a series of thick film samples grown on the Au(111) using increasingly degassed powders. The UPS spectrum shown in the paper corresponds to the thick film obtained after the described purification procedure. The UPS spectra were measured by using a Scienta SES-100 hemispherical analyzer and the He(II) line ($h\nu$ = 40.8 eV) from a Gammadata/Scienta VUV 5000 microwave-driven monochromatized He discharge lamp. Binding energy (BE) calibration was performed by measuring the Fermi level of the clean substrate right before growing the thick films. Although all contaminants were successfully removed, also the powders were depleted of the molecule of interest since melem slowly polymerizes close to the sublimation temperature. As a consequence, gas phase measurements were performed with a low molecular flux affecting the overall statistics of the spectra. Moreover, all gas-phase spectra reveal the presence of gaseous ammonia, a subproduct of the condensation reaction. The N 1s XPS spectrum of gaseous melem was acquired with a Scienta SES-200 hemispherical analyzer with photon energy of 495 eV and energy resolutions of 220 meV. The photoelectron energy calibration was made by measuring the reference N 1s level of gaseous N$_2$ (409.9 eV).[23] Valence level spectra were acquired with a photon energy of 40 eV and energy resolution of 50 meV. The ionization energy scale calibration was performed by introducing Ar and measuring the reference 3p$_{3/2}$ line (15.76 eV).[23] The N K-edge NEXAFS spectrum was measured in total ion yield mode (TIY) with a photon energy resolution set to 55 meV. The photon energy scale calibration was provided by simultaneous acquisition of the N K-edge NEXAFS spectrum of gaseous N$_2$ and locating the π^* second vibrational resonance (ν' = 1) at 401.10 eV.[24] The absorption intensity was normalized with the transmitted photon flux measured by a calibrated Si photodiode.

Core-level spectra for 1 monolayer (ML) melem/Au(111) were measured at the ALOISA beamline. Melem was sublimed from a boron nitride crucible held at the temperature of about 573 K. In this case, powders were not completely purified before measurements. The monolayer saturation coverage was determined by multilayer deposition followed by a flash to 473 K for thermal desorption of second layer molecules and contaminants. The monolayer used for the present study was then obtained by incremental deposition of fractional monolayer amounts and shortly flashed to 473 K after the last deposition (to remove contaminants). The N 1s XPS spectra were acquired at normal emission and grazing incidence (4°) with a photon energy of 515 eV (overall resolution ∼150 meV). The binding energy scale was calibrated by setting the Au 4f$_{7/2}$ peak to the reference binding energy of 84.0 eV. NEXAFS measurements were performed at N K-edge in the partial electron yield (PEY) mode (resolution 80 meV) by means of a channeltron equipped with a grid polarized to −370 V to reject low energy secondary electrons. The orientation of the surface with respect to the linear polarization of the photon beam was changed from transverse magnetic (TM, closely p-polarization) to transverse electric (TE, s-polarization) by sample rotation around the photon

beam axis while keeping a constant grazing angle of 6°. Details about calibration and normalization of the NEXAFS spectra can be found in refs 25 and 26. Both gas phase and solid state N 1s XPS spectra were fitted by using Voigt profiles having common Lorentzian (0.10 < L < 0.13 eV)[27] and Gaussian broadening.

Computational Methods. All the calculations reported in this work were carried out within the DFT framework, using the QuantumESPRESSO suite.[28−30] The ground state calculations were performed using the PBE exchange-correlation functional,[31] with a cutoff of 46 and 364 Ry on the wave function and charge-density plane waves basis set, respectively. The dispersion interactions were included through the Grimme-D3 correction.[32] In the case of periodic models, the calculations were performed by considering a shifted Monkhorst−Pack 4 × 4 × 1 grid of k-points in the reciprocal space. For the calculation of the density of states (DOS), the k-point grid was expanded to 12 × 12 × 1. The model structures including the metal surface were constructed by optimizing a supercell containing one or two melem molecules and a slab made from the 3 × 3 or 5 × 5 repetition of the Au(111) unit cell, depending on the H-bonding motif. The slabs contain three layers of Au atoms, with a crystal structure taken from that of the bulk Au, with an optimized Au lattice of 4.16 Å (experimental value 4.08 Å[33]); only the coordinates of the topmost two layers (and those of melem) were relaxed. In order to build the supported 2D systems, we used the information from a preliminary investigation on the adsorption of an isolated molecule on Au(111) (such as best adsorption sites, rotational domains, etc.). We considered the same patterns of the optimized unsupported 2D networks, and we enlarged their unit cell, matching the (fixed) size of the Au(111) supercells. For the isolated molecule only, the electronic structure of the ground state was calculated also with the B3LYP[34,35] exchange and correlation functional: in that case, a plane wave basis set size of 70 Ry was considered.

The XPS spectra were calculated through the ΔSCF method,[36] i.e., by placing a modified pseudopotential hosting a N 1s core hole at every N atom, then taking the total energy difference from a chosen reference in order to calculate the core level shift (CLS). In this work, the total energy of the pyridinic N was assumed as reference for the CLSs. In this case, the plane waves' cutoff was increased to 66 Ry; the final spectra were obtained through the convolution of the delta-like CLSs with Gaussian functions, with a broadening σ = 0.17 eV.

The NEXAFS spectra were calculated through the transition-potential method,[37] using pseudopotentials generated with a half core hole; in these cases, the plane wave basis set was enlarged to 61 Ry. The absorption cross section was calculated by the XSpectra code,[38] included in the QuantumESPRESSO suite. The final spectra were obtained with a linear broadening of 0.2 eV.

RESULTS AND DISCUSSION

Electronic Characterization of Isolated Melem and Unsupported H-Bonded Networks. As shown in previous STM studies,[20−22,39] melem molecules adsorb planar on surfaces like Au(111) and Ag(111) forming a variety of different, mostly coexisting, hydrogen-bonded networks. All structures feature two basic intermolecular H-bond patterns, which are usually denoted as side-by-side (SS) and head-to-tail (HT) (see Figure 1 panels a and b, respectively). In the side-by-side motif, a double H-bond of the type −NH···N occurs
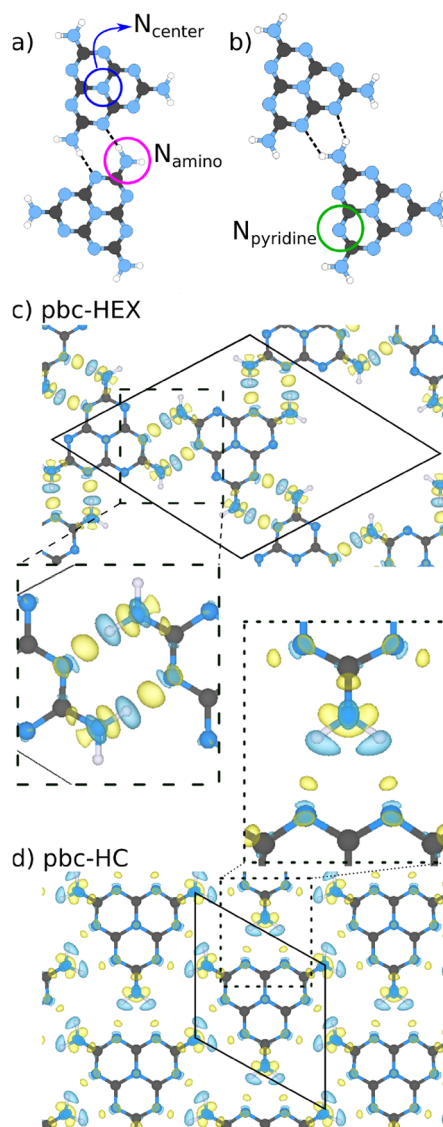

Figure 1. (a,b) Top view of two different H-bond patterns, side-by-side (a) and head-to-tail (b). The different N-containing species are shown as well; the H-bonds are represented through dashed lines. (c,d) Top view of the optimized unsupported 2D pbc-HEX and pbc-HC models. For both structures, a box shows a zoom in around H-bonding atoms. The electronic charge density redistribution due to the formation of a periodic H-bonds network is highlighted through yellow/cyan lobes (electron accumulation/depletion). Isovalues: 0.003 e−/Å³. C, N, and H atoms are represented by gray, blue, and white spheres, respectively. In panels c and d the supercell structures are shown with a solid line.

between two adjacent melem molecules each of them providing one hydrogen of the amino group (−NH₂) and one pyridine-like nitrogen (−C≡N−). In the head-to-tail arrangement, a similar double H-bond is formed by connecting both amine H of one molecule with two neighboring heterocycle aromatic N. In order to best describe the behavior of the different melem networks self-assembled on the metal surface, we optimized two prototypical configurations whose geometries are based on those of commensurate melem/ Au(111) structures derived from the STM studies. The first one, which we label pbc-HEX, originates from the SS pattern and yields low-density domains exhibiting hexagonal nano-
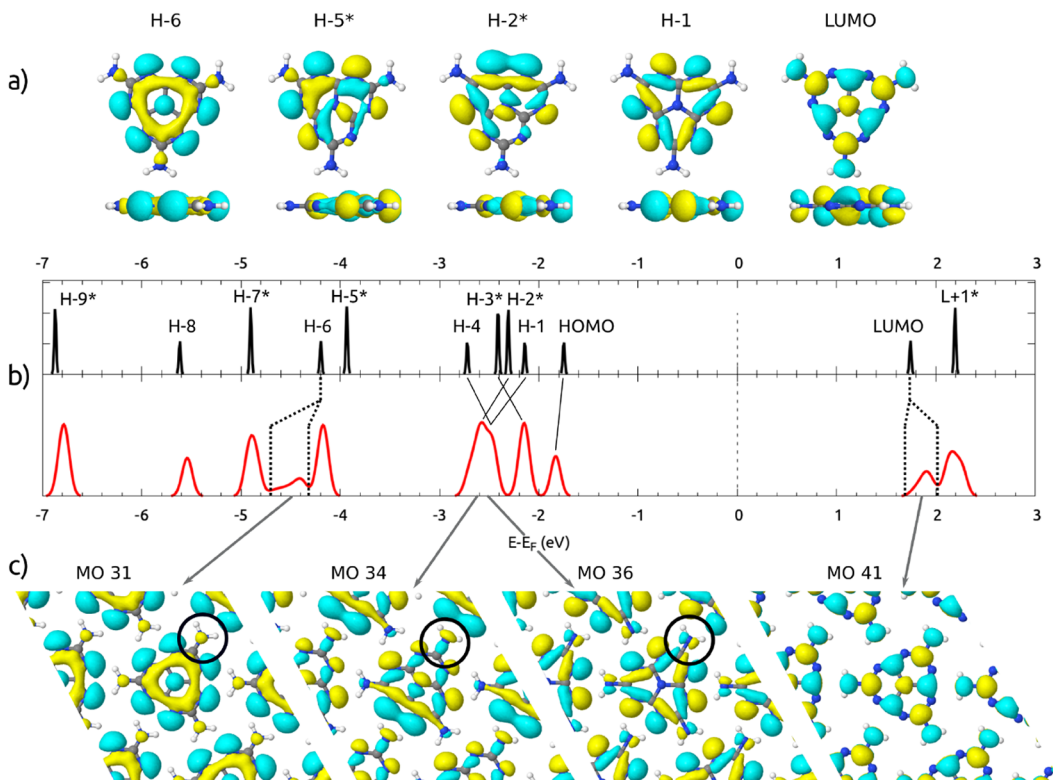
Figure 2. Panel a: charge density distribution ρ of a few selected molecular orbitals (MOs) of molecular melem. The asterisk (∗) in the label marks a doubly degenerate state. Panel b: comparison between the energy position of the eigenstates of the isolated molecules (black lines) and density of states of the optimized pbc-HC model (red curve). In the case of HOMO−6 and LUMO, which form small bands in pbc-HC (see Figure S4 for details), the black dotted lines mark the edges of such bands. Between −3 and −2 eV below E_F, the solid lines mark those states with changed energy order/position after the self-assembly of the molecules. Panel c: ρ calculated at the Γ point for the eigenstates of the pbc-HC model derived from the MOs shown in panel a, and now labeled through their computational index MO(i) (e.g., the lowest unoccupied orbital MO41 derives from the molecular LUMO). Panels a and c: isovalue 0.003 e$^-$/Å^3. Yellow or cyan lobes color the phase dependent isosurface. C, N, and H atoms are represented by gray, blue, and white spheres, respectively. The black circles highlight the modifications on the ρ of pbc-HC MOs due to the formation of H-bonds.

pores. The second configuration, which we label pbc-HC, represents monomers assembling through the HT motif, yielding a denser close-packed arrangement with honeycomb structure. A schematic of the pbc-HEX and of the pbc-HC networks is given in Figure 1 panels c and d, respectively.

In this section, we present, for the first time, a detailed study of the electronic structure of H-bonded melem systems by simulating the unsupported pbc-HEX and the pbc-HC networks. Figure 1c,d shows 2D plots representing the electronic charge density difference between the isolated and the H-bonded melem, both in the pbc-HEX and the pbc-HC models. As expected, the plots evidence significant charge density redistributions in correspondence of the H-bonds. Regions of charge depletion are mostly localized on the H atoms. On the other hand, charge accumulation mainly occurs just aside the N_{amino} and, to a minor extent, in the space between the H and the $N_{pyridine}$ atoms (for a definition of the different types of N atoms, see Figure 1a,b). Minor charge depletions are predicted on the N_{amino} and $N_{pyridine}$ atoms.

Although similar charge density difference plots are commonly used for describing H-bonded networks,[40,41] there are no detailed studies correlating such electronic charge redistributions with the modifications that each molecular orbital (MO) undergoes due to the H-bond formation. Hence, in order to verify whether specific molecular orbitals go through any major perturbation, the MOs of both the isolated

and the H-bonded melem were analyzed and compared. Since the pbc-HEX structures have two molecules per unit cell, their eigenstates can be grouped into almost degenerate pairs. Each pair can be regarded as the linear combination (in-phase and out-of-phase) of the MOs of a single melem molecule in the pbc-HC repeating unit, as shown in the Supporting Information file Figure S1a. Based on this recognized analogy, for an easier inspection and to have a one-to-one correspondence with the isolated monomer, in the following we will focus the attention only on the MOs of pbc-HC. This choice is also supported by the similarity of the spectroscopic results simulated for pbc-HC and pbc-HEX structures, as shown in Figure S1b−d.

The charge density distribution (ρ) of the most relevant MOs of the isolated molecule is shown in Figure 2a, while the corresponding MO energy positions, calculated at the PBE level, are reported in the upper panel of Figure 2b (double degenerate states are marked with an asterisk ∗); for comparison, the (PBE) density of states (DOS) calculated for the periodic melem network pbc-HC is shown in the lower panel of Figure 2b. The ρ calculated for selected eigenstates of pbc-HC is reported in Figure 2c.

The MOs of the periodic model, which we label MO(i), where i is the index of the corresponding eigenstate, strongly resemble those of the isolated molecule (for a full comparison of all MOs, both those of the gas phase melem and those of the

unsupported pbc-HC model, see Figure S2). We may notice some modifications for the lone-pair σ-orbitals, which are indeed the MOs mostly involved in the in-plane H-bonding interactions. For instance, the σ-symmetry MO36, which clearly derives from HOMO−1 (Figure 2a), unambiguously shows new in-plane charge density aside the N_{amino} atoms (black circle in Figure 2c); a similar effect is found for the HOMO−2* → MO(35−34). A slightly different situation is observed for HOMO−5 → MO(33−32) (see Figure S2) and HOMO−6 → MO31 (Figure 2a/c): in the isolated molecule, these orbitals already bear some charge density in between the C to N_{amino} bond. In the corresponding pbc-HC MOs, the charge density is enhanced and clearly displaced toward the N_{amino} atom. Such modifications well correlate with the charge density redistributions shown in Figure 1d, in particular with the in-plane accumulation around the N_{amino}.

In comparison with the isolated molecule, the analysis of the DOS of the periodic pbc-HC model (both reported in Figure 2b) reveals additional effects correlated with the formation of a melem network and H-bonds: while the state at the top of the valence band (MO40) still corresponds to the HOMO of the molecule, there is a rearrangement of states in the region between −3 and −2 eV, as highlighted in Figure 2b. In particular, we observe that the interaction experienced by the sp^2 states of the $N_{pyridine}$ lone pairs, as due to the H-bonds, stabilizes the original HOMO−1 and HOMO−2* of the molecule into the MO36 and MO35/34 of pbc-HC, respectively. On the contrary, the π-type MO37, MO38, and MO39 of pbc-HC, which are more localized on the $N_{pyridine}$ atoms, are shifted toward higher energies with respect to their molecular counterparts HOMO−4 and HOMO−3* (see Figure S3 for more details on the projection of the DOS on different atomic orbitals of our models).

Comparison of the Theoretical DOS with the Experimental UPS Data. Experimentally, direct probing of the valence levels can be performed by using ultraviolet photoemission spectroscopy (UPS). Figure 3a shows the comparison between the UPS spectrum of the gaseous melem along with the position in energy of the eigenvalues calculated for the isolated molecule, both at the PBE and B3LYP level. The theoretical PBE curve is further decomposed in two atomic contributions: the projection on all $N_{pyridine}$ atomic orbitals and N_σ, i.e., the projection on the σ-bonding orbitals of all N atoms (see Figure S3 for further details). In order to verify the reliability of our results calculated by the PBE functional, we simulated the electronic structure of the isolated molecule with the B3LYP functional (dashed gray area in Figure 3a), which is known to be less affected by the energy scale shrinking, as reported in refs 42 and 43. Except for minor differences, the overall progression of the eigenvalues is respected, proving that the PBE functional does not alter the chemistry of the system.

Similar to the case of the heptazine molecule $(C_6N_7H_3)$,[44] in the isolated melem the self-standing peak *a* at 8.2 eV is assigned to the HOMO level, indicating that in both molecules there is a non-bonding π orbital exclusively localized on the pyridine N. The HOMO level is followed by a structureless region (peak *b*) of high photoelectron intensity at ca. 9.5 eV that arises from the three highest occupied lone-pair orbitals (HOMO−1, HOMO−2*) plus three occupied π orbitals (HOMO−3*, HOMO−4). Although the overlap with the vibrational progression of the NH_3 3a1 state at ca. 10.5 eV[23] (see experimental details), peak *c* can be clearly assigned to
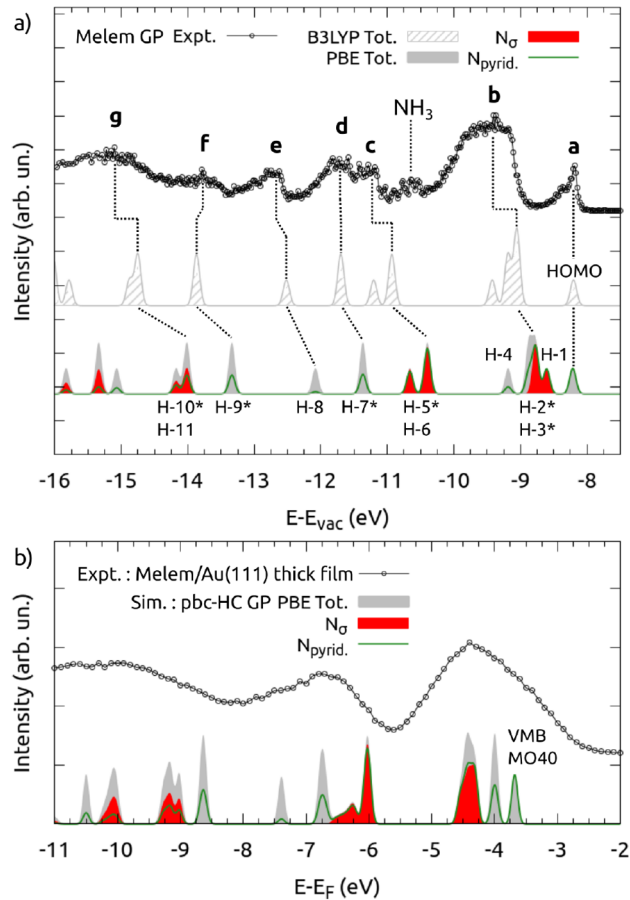

Figure 3. Comparison between the experimental UPS spectra and the simulated DOS, along with the projections on selected atomic orbitals: the gas phase (GP) melem (a) and H-bonded systems (b). The calculated DOS are aligned to the experimental data in order to match the measured position of the valence band maximum (VBM) or that of the HOMO.

three deeper lone-pair orbitals (HOMO−5*, HOMO−6) and peak *d* with the doubly degenerate π HOMO−7*.

For the unsupported H-bonded system, we compare the theoretical DOS with the experimental UPS spectrum measured for a thick film of melem grown on Au(111) (Figure 3b). In this case, we assume that the thickness of the deposited melem multilayer allows for a direct comparison of the deposited topmost layers with the unsupported periodic model. Despite the fair agreement between the experimental and calculated curves, the huge broadening overwhelming the UPS spectrum does not allow to extract any specific information regarding the fine modifications induced by the H-bonds formation.

Electronic Characterization of Melem(1 ML)/Au(111). To validate the predicted H-bonding effects (i.e., charge density redistributions) we characterized our systems by other spectroscopic techniques, such as XPS and NEXAFS, which are proven to be more sensitive to the local electronic state of the heteroatoms involved in this type of interactions.[16,45] To this aim, core-level spectra were measured for both the gaseous melem and one monolayer grown on the relatively inert Au(111) surface.

The gas-phase data are compared with those calculated for the isolated molecule. For the periodic network, the properties

of one monolayer of melem deposited on the Au(111) surface, melem(1 ML)/Au(111), are simulated using the pbc-HC model, either unsupported or supported on the Au(111) surface (with a structure commensurate to that of the metal). This two-step modeling (unsupported and supported) was fundamental in order to evaluate any possible surface-induced perturbation of the H-bonded system.

Comparison of Experimental and Simulated XPS Spectra. In Figure 4 we report the N 1s XPS spectrum for the gaseous
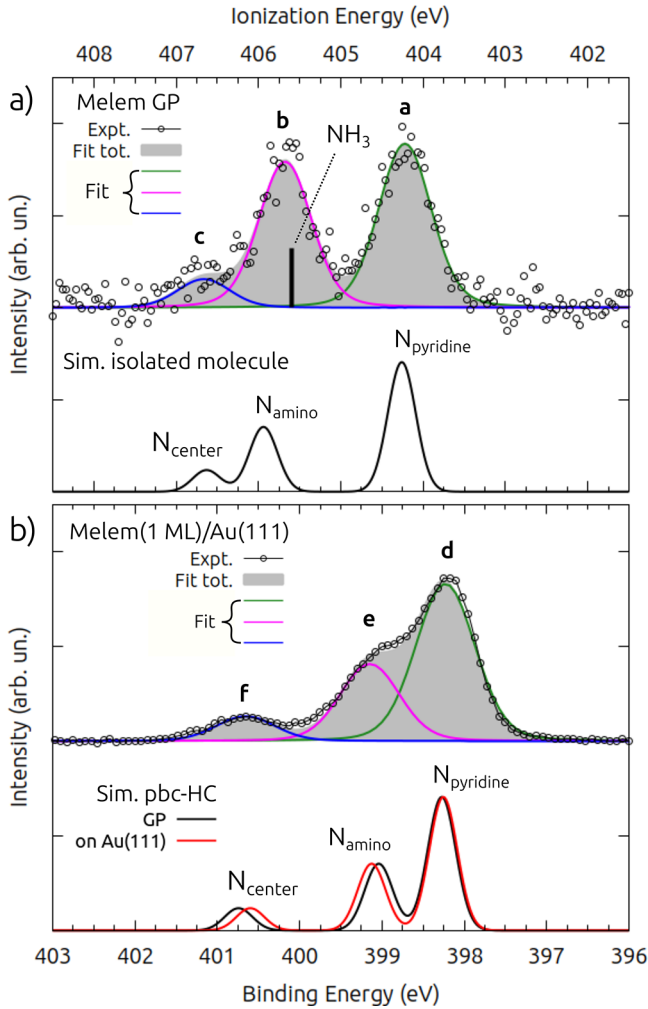

Figure 4. Experimental and simulated XPS N 1s spectra for gas phase (GP) melem (panel a) and for 1 ML of melem deposited on Au(111) (panel b). For the experimental curves, the components resulting from fitting the data are shown as well with green, magenta, and blue lines. In the case of the pbc-HC model, the spectra for both the unsupported and supported cases are shown. For the GP melem, the energy position of the NH_3,[46] which is a contaminant to the system, is marked by the black stick. The simulated spectra are aligned to the experimental ones in order to match the position of the most intense ($N_{pyridine}$) peak.

melem and the 1 ML sample. The gas phase spectrum clearly shows two main peaks at 404.2 eV (peak *a*) and 405.7 eV (peak *b*), and a smaller one at 406.7 eV (peak *c*). The *a*:*b*:*c* intensity ratio is found equal to 5.8:5.1:1 suggesting that peak *a* can be associated with the N 1s level of the six $N_{pyridine}$ and peak *c* with that of the N_{center}. The assignment is confirmed by theoretical calculations, where the energy separation between N_{center} and $N_{pyridine}$ is ca. 2.4 eV, i.e., very close to the

experimental core level shift (CLS) of 2.5 eV. At the same time, peak *b* is found at +1.5 eV from peak *a*, in good accordance with the theoretical CLS of the N_{amino} (1.7 eV). However, the intensity of peak *b* is clearly enhanced by the presence of NH_3, whose N 1s ionization energy at ~405.6 eV (marked as a black stick in Figure 4) is very close to that of the N_{amino}.[16,46]

The spectrum of 1 ML sample features three main peaks at 398.2 eV (*d*), 399.1 eV (*e*) and 400.7 eV (*f*), with intensity ratio *d*:*e*:*f* = 6.5:3.1:1 that now better compares with that expected from the stoichiometry of the molecule (ammonia does not stick on the gold surface at room temperature).[47] Slight deviations can derive from photoelectron diffraction effects[17] or persistent contaminants (see experimental method for sample preparation). Interestingly, the CLS of the N_{center} is found equal to the gas phase value (~2.5 eV) while that of the N_{amino} significantly decreases from 1.5 to 0.9 eV. The same effect is observed in theoretical data, where the calculated CLS of N_{center} is 2.6/2.4 eV for the unsupported/supported models, respectively, and that of N_{amino} decreases to 0.8/0.9 eV. This result clearly reflects the electronic charge density redistributions due to the H-bonds formation (see Figure 1) and, in particular, the electron accumulation around the N_{amino}. Despite the good agreement between the experimental and simulated XPS spectra, the resolution in the measurements does not allow to distinguish between contribution from the suspended and the supported layer. The observed differences in the CLS data may be indicative of a weak molecule−substrate interaction that will be discussed below.

Comparison between Experimental and Simulated NEXAFS Spectra. Another technique that is extremely sensitive to the molecule−molecule interaction is the NEXAFS spectroscopy. Figure 5 shows both the experimental and the calculated N K-edge NEXAFS spectra of melem in the gas-phase and when embedded within H-bonded domains on Au(111). Solid state measurements were performed in two different scattering geometries, the s-polarization (s-pol, electric field vector E parallel to the surface plane) and the p-polarization (p-pol, electric field vector E almost perpendicular to the surface plane). As melem adsorbs flat, enhancement of π^* and σ^* resonances occur in p-pol and s-pol, respectively. Theoretical spectra of the pbc-HC models are then calculated resolving both π^* and σ^* resonances, providing a general sound agreement with the experimental curves. Regarding gas phase measurements, four main features are observed in Figure 5a. Three of them, peak *a* (~399.7 eV), peak *b* (~402.4 eV), and peak *c* (~403.2 eV) can be reasonably assigned to resonances of the molecule. Conversely, the fourth structured feature at around 401 eV clearly belongs to N_2[24] (background gas inside the UHV chamber). According to our theoretical results, peak *a* can be assigned to a π^* transition from the $N_{pyridine}$ 1s level to the double degenerate LUMO+1 and, marginally, to the LUMO, which we label $L+1_{py}$ and $LUMO_{py}$, respectively, in Figure 5a. On the other hand, peak *b* may stand for the π^*-resonances involving the LUMO mostly localized on the N_{amino} and N_{center} atoms ($LUMO_{am}$ and $LUMO_{cen}$) as well as a higher energy empty state localized on $N_{pyridine}$ atoms (observed at ~402.5 eV, not marked in the figure). Lastly, the broad feature observed at ~403.2 eV (*c*) can be assigned to excitations to σ^* states localized on N_{amino} atoms (σ^*_{am}). For additional details on the calculated N species-dependent components of the NEXAFS and the π-like or σ-like projections of the DOS, see Figures S3 and S5. It has to be
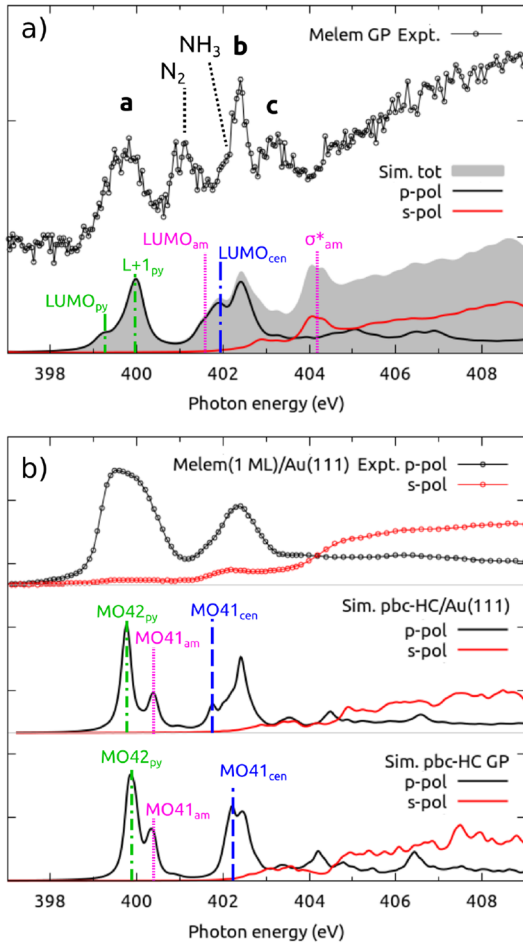
Figure 5. Experimental and simulated NEXAFS spectra for gas phase (GP) (panel a) and 1 ML of melem deposited on Au(111) (panel b). The experimental solid-state spectrum is compared with that calculated for the both unsupported and supported pbc-HC model. Both results for p- and s-polarization of the incident light are reported (black and red lines, respectively). When possible, the absorption features are marked with lines indicating the involved empty molecular orbitals (MO): the subscripts refer to the N atom at which the photoexcitation occurs. The simulated spectra are aligned to the experimental ones in order to match the position of the first resonance.

noted that the most intense NH_3 resonance (402.2 eV)[48] is likely overlapping with feature *b*.

In the case of the self-assembled, supported or unsupported networks, two main modifications are observed. First of all, the first π^* resonance in the experiment is visibly broader with respect to that in the gas phase. According to our simulated results, indeed, two main resonances are now contributing to this first peak, i.e., those labeled $MO42_{py}$ and $MO41_{am}$ in Figure 5b, but originating at different N atoms. The former is located on $N_{pyridine}$ and is the most intense transition, similar to the LUMO+1 resonance observed in the spectrum simulated for the isolated molecule. The second transition ($MO41_{am}$) is now originating from N_{amino} atoms and can be associated with the red-shifted $LUMO_{am}$ resonance of the NEXAFS spectrum of GP melem. This finding is in line with the CLS reduction between the $N_{pyridine}$ and N_{amino} 1s levels already observed in the XPS measurements. A second modification concerns the vanishing of the σ^* resonances (σ^*_{am}) located at 403.2 eV

(peak *c*) in the gas phase spectrum, involving the N_{amino}. The quenching of this type of resonances has already observed for other H-bonded systems (cyanuric acid,[49] melamine,[16] and ice[50]) and derives from the strong modifications undergone by the involved antibonding MOs (usually localized on the X-H terminations).

Dipolar Out-of-Plane Interactions. So far we have focused our attention on the formation of H-bonds between melem molecules, assuming the substrate as an inert support allowing the self-assembly of the network. We now complete our investigation by studying the effect of the metal surface on the electronic structure of the H-bonded molecules.

We have indeed observed some evidence of the interaction between the adsorbed melem molecules and the Au(111) surface, mainly in the XPS spectra (Figure 4, lower panels), where the calculated contributions of the N_{amino} and N_{center} with or without the metal support are slightly different. In particular, the CLS of N_{amino} in the unsupported case is smaller (0.8 eV) than the supported case (0.9 eV), while for N_{center} the CLS calculated for the unsupported case is larger (2.6 vs 2.4 eV). Since the melem network self-assembles in a flat configuration, we can expect these differences to arise from localized charge rearrangements on the different N species triggered by the surface, as shown in Figure 6a. In correspondence of all C and N atoms a pattern of electronic depletion can be observed, resembling the p_z orbitals, while some charge accumulation can be observed at the interface with the substrate: this result seems to suggest some degree of electron transfer from the molecule to the metal. In order to investigate further the potential source of the rearranged electrons, we calculated the projected DOS onto both N p_z and C p_z atomic orbitals for the pbc-HC models and we performed their energy integration, which represents the total number of electrons $N_e(E)$ occupying such states. Figure 6b shows the comparison of the $N_e(E)$ curves calculated for both the supported and the unsupported networks revealing that there is no net transfer of charge. In order to improve the accuracy of the calculated total charges, we performed the Bader analysis[51,52] on the system, which confirms the result obtained through the Löwdin projections.[53]

Therefore, we conclude that the effect of the metallic surface on the molecular network is to polarize the interface, where the electrons of the melem occupying the π states are attracted toward the metal without being properly transferred to Au states. Since the local dipole is affected by the interaction of the specific atom with both the overall π system and the Au atoms below, some minor differences in the electron screening experienced by the core excited electron are expected, therefore explaining the differences between the calculated N 1s XPS spectra of the supported and unsupported networks.

■ CONCLUSION

In this work, we performed a combined experimental and theoretical investigation of the electronic structure of a self-assembled layer of melem molecules deposited on the weakly interacting Au(111) surface. We characterized the samples by means of UPS, XPS, and NEXAFS spectroscopies, whose results were then compared with the charge density, the electronic structure, and the spectroscopic data calculated with DFT methods from computational models.

The theoretical results show good agreement with the experimental characterization of the samples and provide electronic and atomistic details on the H-bonding intermo-
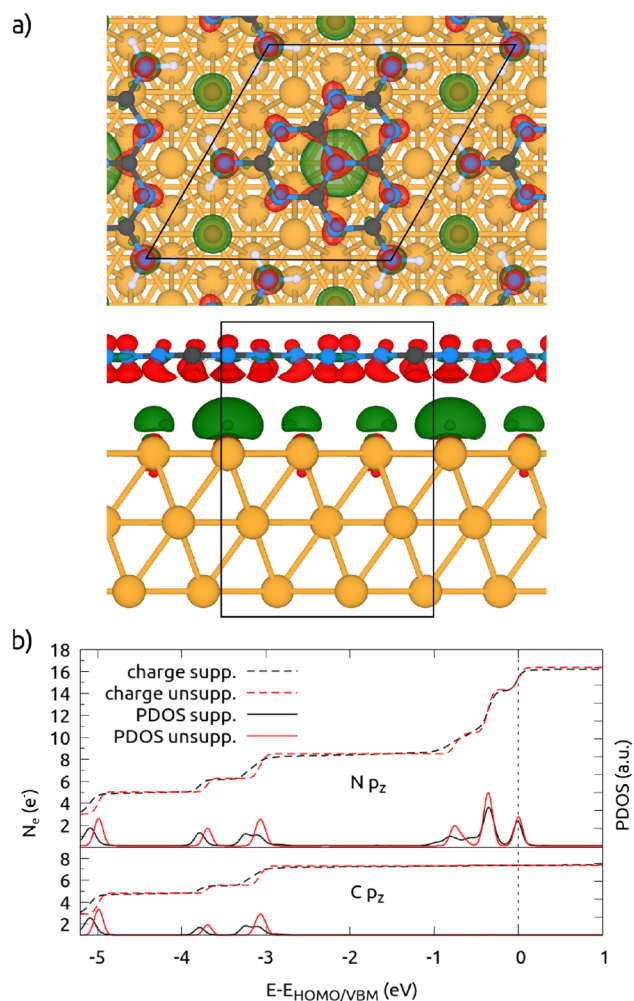
Figure 6. Panel a: top and side views of the pbc-HC/Au(111) model, along with the charge rearrangement due to the presence of the interface. Green/red lobes indicate electron accumulation/depletion, respectively. Isovalue: 0.0003 e⁻/Å³. C, N, H, and Au atoms are shown with blue, gray, white, and orange spheres, respectively. The supercell structure is shown with black lines. Panel b: comparison between the DOS projected on the N p_z or C p_z atomic orbitals (solid lines) and the energy-dependent total number of electrons Ne occupying those states (dashed lines) for the supported or the unsupported pbc-HC model.

lecular interaction. We find strong evidence that only non-covalent bonding occurs between the amino and pyridinic N atoms. First, in the DFT calculations we observe some rearrangement of the electronic charge distribution but no formation of additional bonding orbitals. Second, for both experimental and theoretical XPS spectra, the observed BE shifts of the different N components (in particular a reduction of the CLS of N_{amino} from 1.5 to 0.9 eV) agree with a dipolar interaction between H-bonded fragments in the 2D network, where the N_{amino}, acting as H donor, experiences some local electronic charge accumulation. This BE red-shift also coherently affects the appearance of the theoretical and experimental NEXAFS spectra. We find that these results, both experimental and theoretical, are independent from the specific H-bonding motif in the 2D periodic networks.

Finally, we complemented our study by investigating the role of the metallic substrate on the properties of the self-assembled molecular layer, through the comparison between the supported and the unsupported models. We find that the weak interaction with the Au(111) surface prevents a net charge transfer from the molecules, but only allows for a polarization of the electronic charge in the π states at the interface.

■ **AUTHOR INFORMATION**

Corresponding Authors

Valeria Lanzilotto − *Dipartimento di Chimica, Sapienza Università di Roma, 00185 Roma, Italy; IOM-CNR, Istituto Officina dei Materiali, 34149 Trieste, Italy;* Present Address: Dipartimento di Scienze Chimiche e Farmaceutiche, Università di Trieste, Via Licio Giorgieri 1, 34127 Trieste, Italy; orcid.org/0000-0001-7132-6380; Email: valeria.lanzilotto@units.it

Cristiana Di Valentin − *Department of Materials Science, Università degli Studi di Milano-Bicocca, 20125 Milano, Italy;* orcid.org/0000-0003-4163-8062; Email: cristiana.divalentin@unimib.it

Authors

Aldo Ugolotti − *Department of Materials Science, Università degli Studi di Milano-Bicocca, 20125 Milano, Italy;* orcid.org/0000-0002-4894-070X

Cesare Grazioli − *IOM-CNR, Istituto Officina dei Materiali, 34149 Trieste, Italy;* orcid.org/0000-0002-6255-2041

Luca Schio − *IOM-CNR, Istituto Officina dei Materiali, 34149 Trieste, Italy*

Jorge Manuel Zamalloa-Serrano − *ESISNA Group, Instituto de Ciencia de Materiales de Madrid (ICMM-CSIC), 28049 Madrid, Spain;* orcid.org/0000-0002-0569-2099

Matus Stredansky − *IOM-CNR, Istituto Officina dei Materiali, 34149 Trieste, Italy; Department of Physics, University of Trieste, 34127 Trieste, Italy*

Teng Zhang − *Department of Physics and Astronomy, Uppsala University, 751 20 Uppsala, Sweden;* Present Address: School of Integrated Circuits and Electronics, MIIT Key Laboratory for Low-Dimensional Quantum Structure and Devices, Beijing Institute of Technology (BIT), 100081 Beijing, China.; orcid.org/0000-0001-8739-7773

Monica de Simone − *IOM-CNR, Istituto Officina dei Materiali, 34149 Trieste, Italy;* orcid.org/0000-0002-9491-0173

Lorenzo Ferraro − *Department of Materials Science, Università degli Studi di Milano-Bicocca, 20125 Milano, Italy*

Luca Floreano − *IOM-CNR, Istituto Officina dei Materiali, 34149 Trieste, Italy;* orcid.org/0000-0002-3654-3408

Marcello Coreno − *ISM-CNR, Istituto di Struttura della Materia, Trieste 34149, Italy*

Carla Puglia − *Department of Physics and Astronomy, Uppsala University, 751 20 Uppsala, Sweden;* ⊙ orcid.org/0000-0001-6840-1570

Notes

The authors declare no competing financial interest.

◼ REFERENCES

(1) Wang, X.; Maeda, K.; Thomas, A.; Takanabe, K.; Xin, G.; Carlsson, J. M.; Domen, K.; Antonietti, M. A metal-free polymeric photocatalyst for hydrogen production from water under visible light. *Nat. Mater.* **2009**, *8*, 76−80.

(2) Banerjee, T.; Podjaski, F.; Kröger, J.; Biswal, B. P.; Lotsch, B. V. Polymer photocatalysts for solar-to-chemical energy conversion. *Nature Reviews Materials* **2021**, *6*, 168−190.

(3) Ashworth, C. Going organic. *Nature Reviews Materials* **2020**, *5*, 561.

(4) Bai, Y.; Wilbraham, L.; Slater, B. J.; Zwijnenburg, M. A.; Sprick, R. S.; Cooper, A. I. Accelerated Discovery of Organic Polymer Photocatalysts for Hydrogen Evolution from Water through the Integration of Experiment and Theory. *J. Am. Chem. Soc.* **2019**, *141*, 9063−9071.

(5) Lotsch, B. V.; Doblinger, M.; Sehnert, J.; Seyfarth, L.; Senker, J.; Oeckler, O.; Schnick, W. Unmasking Melon by a Complementary Approach Employing Electron Diffraction, Solid-State NMR Spectroscopy, and Theoretical Calculations — Structural Characterization of a Carbon Nitride Polymer. *Chem.—Eur. J.* **2007**, *13*, 4969−4980.

(6) Döblinger, M.; Lotsch, B. V.; Wack, J.; Thun, J.; Senker, J.; Schnick, W. Structure elucidation of polyheptazine imide by electron diffraction—a templated 2D carbon nitride network. *Chem. Commun.* **2009**, *12*, 1541−1543.

(7) Wang, Y.; Vogel, A.; Sachs, M.; Sprick, R. S.; Wilbraham, L.; Moniz, S. J.; Godin, R.; Zwijnenburg, M. A.; Durrant, J. R.; Cooper, A. I.; et al. Current understanding and challenges of solar-driven hydrogen generation using polymeric photocatalysts. *Nature Energy* **2019**, *4*, 746−760.

(8) Fujishima, A.; Honda, K. Electrochemical photolysis of water at a semiconductor electrode. *Nature* **1972**, *238*, 37−38.

(9) Domcke, W.; Ehrmaier, J.; Sobolewski, A. L. Solar Energy Harvesting with Carbon Nitrides and N-Heterocyclic Frameworks: Do We Understand the Mechanism? *ChemPhotoChem.* **2019**, *3*, 10−23.

(10) Ehrmaier, J.; Karsili, T. N.; Sobolewski, A. L.; Domcke, W. Mechanism of Photocatalytic Water Splitting with Graphitic Carbon Nitride: Photochemistry of the Heptazine-Water Complex. *J. Phys. Chem. A* **2017**, *121*, 4754−4764.

(11) Merschjann, C.; Tyborski, T.; Orthmann, S.; Yang, F.; Schwarzburg, K.; Lublow, M.; Lux-Steiner, M.-C.; Schedel-Niedrig, T. Photophysics of polymeric carbon nitride: An optical quasimonomer. *Phys. Rev. B* **2013**, *87*, 205204.

(12) Ugolotti, A.; Di Valentin, C. Trends in excitonic, vibrational and polaronic properties of graphitic carbon nitride polymorphs. *Appl. Surf. Sci.* **2023**, *608*, 155164.

(13) Lau, V. W.-h.; Mesch, M. B.; Duppel, V.; Blum, V.; Senker, J.; Lotsch, B. V. Low-Molecular-Weight Carbon Nitrides for Solar Hydrogen Evolution. *J. Am. Chem. Soc.* **2015**, *137*, 1064−1072.

(14) Lau, V. W.-h.; Moudrakovski, I.; Botari, T.; Weinberger, S.; Mesch, M. B.; Duppel, V.; Senker, J.; Blum, V.; Lotsch, B. V. Rational design of carbon nitride photocatalysts by identification of cyanamide defects as catalytically relevant sites. *Nat. Commun.* **2016**, *7*, 12165.

(15) Lau, V. W.-h.; Yu, V. W.-z.; Ehrat, F.; Botari, T.; Moudrakovski, I.; Simon, T.; Duppel, V.; Medina, E.; Stolarczyk, J.; Feldmann, J.; et al. Urea-Modified Carbon Nitrides: Enhancing Photocatalytic Hydrogen Evolution by Rational Defect Engineering. *Adv. Energy Mater.* **2017**, *7*, 1602251.

(16) Lanzilotto, V.; Silva, J. L.; Zhang, T.; Stredansky, M.; Grazioli, C.; Simonov, K.; Giangrisostomi, E.; Ovsyannikov, R.; De Simone, M.; Coreno, M.; Araujo, C. M.; Brena, B.; Puglia, C. Spectroscopic fingerprints of intermolecular H-bonding interactions in carbon nitride model compounds. *Chem.—Eur. J.* **2018**, *24*, 14198.

(17) Lanzilotto, V.; Grazioli, C.; Stredansky, M.; Zhang, T.; Schio, L.; Goldoni, A.; Floreano, L.; Motta, A.; Cossaro, A.; Puglia, C. Tailoring surface-supported water−melamine complexes by cooperative H-bonding interactions. *Nanoscale Adv.* **2021**, *3*, 2359−2365.

(18) Cometto, C.; Ugolotti, A.; Grazietti, E.; Moretto, A.; Bottaro, G.; Armelao, L.; Di Valentin, C.; Calvillo, L.; Granozzi, G. Copper single-atoms embedded in 2D graphitic carbon nitride for the CO_2 reduction. *npj 2D Materials and Applications* **2021**, *5*, 63.

(19) Ugolotti, A.; Di Valentin, C. Ab-Initio Spectroscopic Characterization of Melem-Based Graphitic Carbon Nitride Polymorphs. *Nanomaterials* **2021**, *11*, 1863.

(20) Bao, M.; Wei, X.; Cai, L.; Sun, Q.; Liu, Z.; Xu, W. Self-assembly of melem on Au(111) and Ag(111): the origin of two different hydrogen bonding configurations. *Phys. Chem. Chem. Phys.* **2017**, *19*, 18704−18708.

(21) Wang, L.; Shi, H.-X.; Wang, W.-Y.; Shi, H.; Shao, X. Identifying the Hydrogen Bonding Patterns of Melamine and Melem Self-Assemblies on Au (111) Surface. *Acta Phys.-Chim. Sin.* **2017**, *33*, 393−398.

(22) Uemura, S.; Aono, M.; Komatsu, T.; Kunitake, M. Two-dimensional self-assembled structures of melamine and melem at the aqueous solution-Au(111) interface. *Langmuir* **2011**, *27*, 1336−1340.

(23) Turner, D. W.; Baker, C.; Baker, A. D.; Brundle, C. R. *Molecular Photoelectron Spectroscopy*; Wiley Interscience: London, 1970.

(24) Sodhi, R. N.; Brion, C. Reference energies for inner shell electron energy-loss spectroscopy. *J. Electron Spectrosc. Relat. Phenom.* **1984**, *34*, 363−372.

(25) Floreano, L.; Cossaro, A.; Gotter, R.; Verdini, A.; Bavdek, G.; Evangelista, F.; Ruocco, A.; Morgante, A.; Cvetko, D. Periodic Arrays of Cu-Phthalocyanine Chains on Au(110). *J. Phys. Chem. C* **2008**, *112*, 10794−10802.

(26) Bavdek, G.; Cossaro, A.; Cvetko, D.; Africh, C.; Blasetti, C.; Esch, F.; Morgante, A.; Floreano, L. Pentacene nanorails on Au(110). *Langmuir: the ACS journal of surfaces and colloids* **2008**, *24*, 767−72.

(27) Nicolas, C.; Miron, C. Lifetime broadening of core-excited and -ionized states. *J. Electron Spectrosc. Relat. Phenom.* **2012**, *185*, 267−272. Special Issue in honor of Prof. T. Darrah Thomas: High-Resolution Spectroscopy of Isolated Species.

(28) Giannozzi, P.; Baroni, S.; Bonini, N.; Calandra, M.; Car, R.; Cavazzoni, C.; Ceresoli, D.; Chiarotti, G. L.; Cococcioni, M.; Dabo, I.; et al. QUANTUM ESPRESSO: a modular and open-source software project for quantum simulations of materials. *J. Phys.: Condens. Matter* **2009**, *21*, 395502.

(29) Giannozzi, P; Andreussi, O; Brumme, T; Bunau, O; Buongiorno Nardelli, M; Calandra, M; Car, R; Cavazzoni, C; Ceresoli, D; Cococcioni, M; Colonna, N; Carnimeo, I; Dal Corso, A; de Gironcoli, S; Delugas, P; DiStasio, R A; Ferretti, A; Floris, A;

Fratesi, G; Fugallo, G; Gebauer, R; Gerstmann, U; Giustino, F; Gorni, T; Jia, J; Kawamura, M; Ko, H-Y; Kokalj, A; Kucukbenli, E; Lazzeri, M; Marsili, M; Marzari, N; Mauri, F; Nguyen, N L; Nguyen, H-V; Otero-de-la-Roza, A; Paulatto, L; Ponce, S; Rocca, D; Sabatini, R; Santra, B; Schlipf, M; Seitsonen, A P; Smogunov, A; Timrov, I; Thonhauser, T; Umari, P; Vast, N; Wu, X; Baroni, S; et al. Advanced capabilities for materials modelling with Quantum ESPRESSO. *J. Phys.: Condens. Matter* **2017**, *29*, 465901.

(30) Giannozzi, P.; Baseggio, O.; Bonfà, P.; Brunato, D.; Car, R.; Carnimeo, I.; Cavazzoni, C.; de Gironcoli, S.; Delugas, P.; Ferrari Ruffino, F.; et al. Quantum ESPRESSO toward the exascale. *J. Chem. Phys.* **2020**, *152*, 154105.

(31) Perdew, J. P.; Burke, K.; Ernzerhof, M. Generalized Gradient Approximation made simple. *Phys. Rev. Lett.* **1996**, *77*, 3865.

(32) Grimme, S.; Antony, J.; Ehrlich, S.; Krieg, H. A consistent and accurate ab initio parametrization of density functional dispersion correction (DFT-D) for the 94 elements H-Pu. *J. Chem. Phys.* **2010**, *132*, 154104.

(33) Jette, E. R.; Foote, F. Precision Determination of Lattice Constants. *J. Chem. Phys.* **1935**, *3*, 605−616.

(34) Becke, A. Density-functional thermochemistry. III. The role of exact exchange. *J. Chem. Phys.* **1993**, *98*, 5648.

(35) Lee, C.; Yang, W.; Parr, R. G. Development of the Colle-Salvetti correlation-energy formula into a functional of the electron density. *Phys. Rev. B* **1988**, *37*, 785−789.

(36) García-Gil, S.; García, A.; Ordejón, P. Calculation of core level shifts within DFT using pseudopotentials and localized basis sets. *Eur. Phys. J.* **2012**, *85*, 239.

(37) Slater, J. C.; Johnson, K. H. Self-Consistent-Field $X\alpha$ Cluster Method for Polyatomic Molecules and Solids. *Phys. Rev. B* **1972**, *5*, 844−853.

(38) Gougoussis, C.; Calandra, M.; Seitsonen, A. P.; Mauri, F. First-principles calculations of x-ray absorption in a scheme based on ultrasoft pseudopotentials: From α-quartz to high-T_c compounds. *Phys. Rev. B* **2009**, *80*, 075102.

(39) Eichhorn, J.; Schlögl, S.; Lotsch, B. V.; Schnick, W.; Heckl, W. M.; Lackinger, M. Self-assembly of melem on Ag(111) - emergence of porous structures based on amino-heptazine hydrogen bonds. *CrystEngComm* **2011**, *13*, 5559.

(40) Silly, F.; Shaw, A. Q.; Castell, M. R.; Briggs, G. A. D.; Mura, M.; Martsinovich, N.; Kantorovich, L. Melamine Structures on the Au(111) Surface. *J. Phys. Chem. C* **2008**, *112*, 11476−11480.

(41) Mura, M.; Martsinovich, N.; Kantorovich, L. Theoretical study of melamine superstructures and their interaction with the Au(111) surface. *Nanotechnology* **2008**, *19*, 465704.

(42) Alippi, P.; Lanzilotto, V.; Paoletti, A. M.; Mattioli, G.; Zanotti, G.; Pennesi, G.; Filippone, F.; Cossaro, A.; Verdini, A.; Morgante, A.; Amore Bonapasta, A. A Ru-Ru pair housed in ruthenium phthalocyanine: The role of a "cage" architecture in the molecule coupling with the Ag(111) surface. *Phys. Chem. Chem. Phys.* **2017**, *19*, 1449.

(43) Ninova, S.; Lanzilotto, V.; Malavolti, L.; Rigamonti, L.; Cortigiani, B.; Mannini, M.; Totti, F.; Sessoli, R. Valence electronic structure of sublimated Fe4 single-molecule magnets: an experimental and theoretical characterization. *J. Mater. Chem. C* **2014**, *2*, 9599−9608.

(44) Shahbaz, M.; Urano, S.; LeBreton, P. R.; Rossman, M. a.; Hosmane, R. S.; Leonard, N. J. Tri-s-triazine: synthesis, chemical behavior, and spectroscopic and theoretical probes of valence orbital structure. *J. Am. Chem. Soc.* **1984**, *106*, 2805−2811.

(45) Garcia-Gil, S.; Arnau, A.; Garcia-Lekue, A. Exploring large O 1s and N 1s core level shifts due to intermolecular hydrogen bond formation in organic molecules. *Surf. Sci.* **2013**, *613*, 102−107.

(46) Bakke, A. A.; Chen, H.-W.; Jolly, W. L. A table of absolute core-electron binding-energies for gaseous atoms and molecules. *J. Electron Spectrosc. Relat. Phenom.* **1980**, *20*, 333−366.

(47) Kay, B. D.; Lykke, K. R.; Creighton, J. R.; Ward, S. J. The influence of adsorbate-absorbate hydrogen bonding in molecular chemisorption: NH3, HF, and H2O on Au(111). *J. Chem. Phys.* **1989**, *91*, 5120−5121.

(48) Wight, G. R.; Brion, C. E. K-shell excitation of CH4, NH3, H2O, CH3OH, CH3OCH3 and CH3NH2 by 2.5 keV electron impact. *J. Electron Spectrosc. Relat. Phenom.* **1974**, *4*, 25−42.

(49) Lanzilotto, V.; Toffoli, D.; Bernes, E.; Stener, M.; Viola, E.; Cossaro, A.; Costantini, R.; Grazioli, C.; Totani, R.; Fronzoni, G. Probing Intermolecular H-Bonding Interactions in Cyanuric Acid Networks: Quenching of the N K-Edge Sigma Resonances. *J. Phys. Chem. A* **2022**, *126*, 6870−6881.

(50) Cavalleri, M.; Ogasawara, H.; Pettersson, L. G.; Nilsson, A. The interpretation of X-ray absorption spectra of water and ice. *Chem. Phys. Lett.* **2002**, *364*, 363−370.

(51) Henkelman, G.; Arnaldsson, A.; Jónsson, H. A fast and robust algorithm for Bader decomposition of charge density. *Comput. Mater. Sci.* **2006**, *36*, 354−360.

(52) Yu, M.; Trinkle, D. R. Accurate and efficient algorithm for Bader charge integration. *J. Chem. Phys.* **2011**, *134*, 064111.

(53) Löwdin, P.-O. On the Nonorthogonality Problem. *Adv. Quant. Chem.* **1970**, *5*, 185−199.